Design and Assessment of a New Active CM Filtering Architecture for PWM Inverter-Fed Motor Drive Systems

Kun Zhang, *Member, IEEE*, Henry Shu-Hung Chung, *Fellow, IEEE*, and Weimin Wu, *Member, IEEE*

***Abstract*—The stepwise common-mode (CM) voltage at the output of inverters causes electromagnetic interference (EMI) and damage to motor bearings. This article proposed a new output active CM filter (ACF) to compensate for the steep rising/falling edges of CM voltage for EMI reduction and bearing protection. An input ACF is also necessary to attenuate the CM noise injected into the grid. Hence, a holistic assessment of input and output ACFs for inverter-fed motor drive systems has been demonstrated. The motor drive system satisfies the CM EMI standard with this new active CM filtering architecture. Ferrite materials and winding configurations of the CM transformer used in the output ACF have been investigated. Moreover, the relationship between the input and output ACFs has been discussed. This article aims to provide new perspectives and implementation guidelines for the ACFs in motor drive systems.**

***Index Terms*—Active filter, bearing, common-mode (CM) voltage, electromagnetic interference (EMI), motor drive.**

I. Introduction

ELECTRIC motors have been widely used in both household and industrial applications. Pulsewidth modulation (PWM) inverters-fed motor drives offer higher efficiency and better performance compared to traditional ones. However, the common-mode (CM) voltage generated by PWM inverters is stepwise; the high *dv/dt* causes CM current through parasitic capacitances, raising concerns of electromagnetic interference (EMI) [1].

A portion of the CM current will flow to the ground through motor bearings. The CM current also generates magnetic flux around the motor shaft and induces a shaft voltage [2], [3]. If this shaft voltage exceeds the insulation of the lubricant film in bearings, a circulating current will flow through a loop of "shaft-bearings-motor frame." High bearing current will damage bearings in the forms of fluting, frosting, pitting, spark tracks, and welding [4], and finally lead to bearing failure. The mitigation methods for bearing failure can be classified into three approaches [5]: first, reinforce the insulation of bearings by using isolated bearings, such as ceramic bearings; second, bypass the bearing with a low-impedance path, such as grounding brushes/rings fabricated with conductive microfibers; third, reduce *dv/dt* by CM filters or cancellation techniques for paralleled inverters [6].

CM filters are most widely used to reduce EMI and protect bearings due to their low cost, robustness, and flexibility [7], [8], [9], [10]. Passive *RLC* filters connected at the output of inverters can effectively reduce *dv/dt*, but their high power loss and bulky volume hinder the advance in power efficiency and density [5].

Active CM filters (ACF) are proposed for compactness by using active filtering techniques. There are two types of ACFs, current-compensation and voltage-compensation. The current-compensation ACFs can achieve high attenuation and compact size [11], [12], [13], especially for the voltage-sensing and current-compensation ACFs, since they do not need transformers in either sensing or compensation stage [12], [13]. However, they circulate the CM current while leaving the CM voltage at motor terminals unchanged; only EMI noise flowing into the grid is attenuated, but the bearings still suffer from the original motor CM current. In such cases, an additional *dv/dt* filter for bearing protection is required. As an advantage, voltage-compensation ACFs alter the CM voltage profiles and, thus, reduce CM noise and protect bearings simultaneously; this makes voltage-compensation ACFs more suitable for motor drive systems.

A feedforward voltage-compensation ACF for motor drives is proposed in [14], and then continuous works have been devoted to advancing this design. Piazza et al. [15] proposed the use of an external power supply and a step-down turns ratio so that low-voltage bipolar junction transistor (BJTs) can be used in high-voltage applications. Darlington pairs are used in the push–pull amplifier to reduce the loading effect. The push–pull amplifier is of class B type, which may have crossover distortion. Feedback voltage-compensation ACFs have also been proposed as an alternative approach [16], [17]; expensive high-voltage operational amplifiers are required

Manuscript received 30 March 2022; revised 27 June 2022 and 19 August 2022; accepted 23 September 2022. Date of publication 28 September 2022; date of current version 18 November 2022. This work was supported by the Research Grants Council from the Hong Kong Special Administrative Region, China, under Grant # CityU 11206219. Recommended for publication by Associate Editor Z. Zhang. *(Corresponding author: Henry Shu-Hung Chung.)*

Kun Zhang and Henry Shu-Hung Chung are with the Centre for Smart Energy Conversion and Utilization Research, Department of Electrical Engineering, City University of Hong Kong, Hong Kong (e-mail: kun.zhang@my.cityu.edu.hk; eeshc@cityu.edu.hk).

Weimin Wu is with the Research Institute of Electronic Automation, Shanghai Maritime University, Shanghai 201306, China (e-mail: wmwu@shmtu.edu.cn).

Color versions of one or more figures in this article are available at https://doi.org/10.1109/TPEL.2022.3210268.

Digital Object Identifier 10.1109/TPEL.2022.3210268

for high-voltage motor drives. Furthermore, integrations of feedforward and feedback ACFs have been proposed to pursue better filtering performance [18], [19].

The prior art voltage-compensation ACFs are full-waveform-compensation filters [14], [15], [16], [17], [18], [19]. They duplicate and then compensate for the entire CM voltage, including both steep edges and high-amplitude plateaus. As a result, this will give challenges to designers to find ways to handle large amounts of power consumption, manage heat dissipation, and increase power density. A high inductance is, thus, required to reduce the operating current and power dissipation of the ACFs [11]. In order to reduce power dissipation and inductance, this article proposes a new edge-compensation ACF that compensates for the rising/falling edges of CM voltage only. Both the CM noise spectrum at the grid interface and the CM current flowing through the motor are reduced.

The filters discussed previously are all connected at the output of inverters; thus, they are called output filters. Since output filters cannot attenuate the CM current leaked from inverters, filters connected at the input of inverters are inevitable and are called input filters.

This article proposed a holistic active CM filtering architecture for motor drive systems, including the input ACF proposed in [20] and the new output ACF. The input ACF is used to attenuate CM noise injected into the grid. The output ACF is primarily devoted to reducing *dv/dt* for bearing protection; it also aids the input ACF to attenuate the CM noise. The CM voltage at the input side is a small disturbance superimposed on the line voltage; its high-frequency component is much lower than the stepwise CM voltage at the output side. Therefore, the input ACF has lower power consumption and smaller volume than the proposed output ACF, which is used to reduce *dv/dt* instead of eliminating CM voltage.

Section II presents the analysis and design procedures of the proposed output ACF. In Section III, the CM performance of the output ACF is evaluated. Ferrite materials and winding configurations of the CM transformer (CMT) used in the output ACF are investigated. A detailed comparison between input and output ACFs have been given.

II. Analysis and Design of the Output Active CM Filter

The proposed output ACF consists of three stages: reference stage, buffer stage, and output compensation stage. It is shown in Fig. 1.

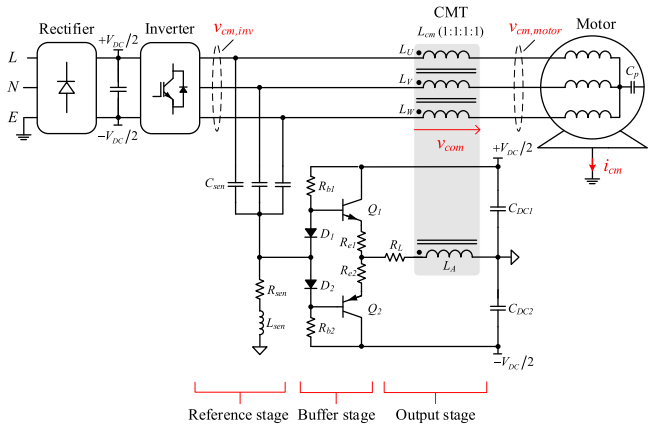

Fig. 1. Schematic diagram of the proposed output ACF.

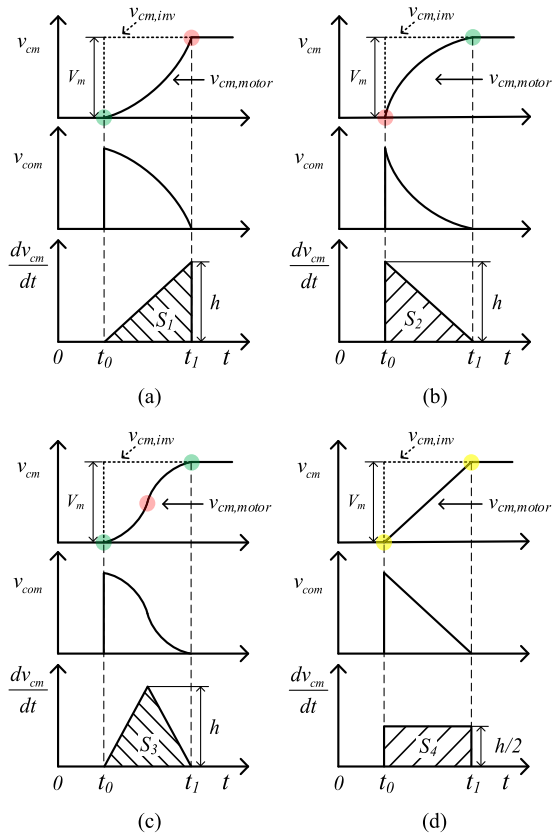

Fig. 2. Four possible waveforms of edge compensation.

A. Design of the Reference Stage

The CMT shown in Fig. 1 has one primary winding (L_A) and three secondary windings (L_U, L_V, and L_W). An edge-compensation voltage v_{com} is applied to the primary winding and then coupled to the secondary windings. Upon compensating the inverter-side CM voltage $v_{cm,inv}$ by v_{com}, the motor-side CM voltage $v_{cm,\mathrm{motor}}$ will have a much smaller *dv/dt*. Fig. 2 shows four possible compensated waveforms. Fig. 2(a) shows a smooth start but a sharp end at the plateau; Fig. 2(b) shows a profile opposite to that in Fig. 2(a); Fig. 2(c) shows a profile having both smooth start and end but a steep rise in the middle; Fig. 2(d) shows a profile having a constant rising slope, which is between the steepest and smoothest ones in Fig. 2(a)–(c).

The integral of $dv_{cm,\mathrm{motor}}/dt$, illustrated by the shaded regions, is the increment of $v_{cm,\mathrm{motor}}$, as expressed in (1). In the four cases, $v_{cm,\mathrm{motor}}$ all rises from zero to V_m during an interval of (t_1 - t_0). Hence, one can conclude $S_1 = S_2 = S_3 = S_4$

$$S = \int_{t_0}^{t_1} \frac{dv_{cm,\mathrm{motor}}}{dt} dt = V_m. \tag{1}$$

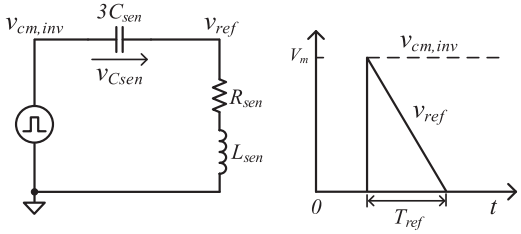

Fig. 3. Equivalent circuit of the voltage reference generator and its voltage waveforms.

Since the time intervals are the same, the peak values of $dv_{cm,\mathrm{motor}}/dt$ in Fig. 2(a)–(c) are identical while that in Fig. 2(d) is one-half of the previous ones. Without loss of generality, more rising patterns exist, and the integrals of $dv_{cm,\mathrm{motor}}/dt$ will remain the same. Based on knowledge of geometry, Fig. 2(d) has the lowest amplitude of $dv_{cm,\mathrm{motor}}/dt$.

The CM current is the displacement current flowing through the parasitic capacitor C_p excited by $v_{cm,\mathrm{motor}}$. The waveforms shown in Fig. 2(d) leads to the lowest peak CM current. Since the damage to bearings is determined by the peak motor CM current [21], [22], a sawtooth compensation voltage is optimal.

The sawtooth voltage is obtained with an *RLC* sensing circuit, as shown in Fig. 1. The values of *RLC* components are designed as follows.

1) C_{sen}*:* Since the sensing capacitors C_{sen} are connected at the output of the inverter, C_{sen} increases the total output capacitance of switching devices and leads to more switching loss. Hence, a small value of C_{sen} is preferred. C_{sen} is chosen to be 100 pF each. A further smaller value might not be sufficient to dominate the effect of the parasitic elements.
2) R_{sen}*:* The equivalent circuit of the voltage reference generator is shown in Fig. 3, and the voltage reference v_{ref} is expressed as

$$L_{sen}C_{sen}\frac{d^2v_{Csen}(t)}{dt^2}+R_{sen}C_{sen}\times\frac{dv_{Csen}(t)}{dt}+v_{Csen}(t)=V_m \tag{2}$$

$$v_{ref}(t)=V_m-v_{Csen}(t). \tag{3}$$

The circuit is a typical second-order system. The step response under different damping factors is illustrated in Fig. 4(a). The damping factor ζ is expressed as

$$\zeta=\frac{R_{sen}}{2\sqrt{L_{sen}/C_{sen}}}. \tag{4}$$

The waveforms of v_{ref} with different ζ are shown in Fig. 4(b). v_{ref} does not decline with an ideal constant slope as the desired waveform shown in Fig. 2(d); it has a long tail. Thus, the reference compensation time T_{ref} is defined as twice $T_{50\%}$ in which v_{ref} drops to one-half of its peak value, i.e., $T_{ref}=2T_{50\%}$. $T_{50\%}$ can be calculated by using the following equation:

$$v_{ref}(T_{50\%})=\frac{1}{2}V_m. \tag{5}$$

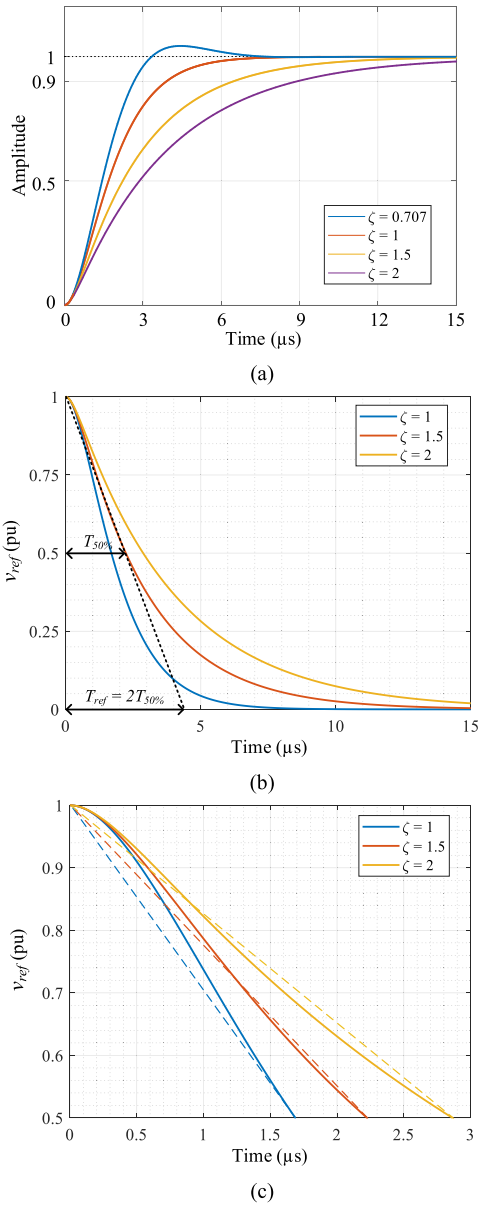

Fig. 4. Waveforms of a second-order system with different ζ. (a) Step responses. (b) Voltage reference v_{ref}. (c) Zoomed waveforms of v_{ref}.

However, (5) is a transcendental equation without a closed-form solution. In order to facilitate the design, the second-order *RLC* circuit is reduced to a first-order *RC* circuit, which has the same waveforms, as shown in Fig. 2(b). Then, (2) is reduced into the form of (6), and T_{ref} is expressed as (7)

$$R_{sen}C_{sen}\frac{dv_{Csen}(t)}{dt}+v_{Csen}(t)=V_m \tag{6}$$

$$T_{ref}=2\ln 2R_{sen}C_{sen}. \tag{7}$$

When T_{ref} is specified to fulfill the specifications of a system, R_{sen} can be derived as

$$R_{sen}=\frac{T_{ref}}{2\ln 2C_{sen}}. \tag{8}$$

It should be noted that (6) is an approximation of (2), and a more accurate solution can be easily obtained by using simulation software. Derived from (6), (8) offers a starting point to fine-tune parameters on a simulator.

3) L_{sen}: L_{sen} is introduced to regulate the response of an *RC* circuit to approach the ideal sawtooth waveform. The sawtooth profile holds only for the initial $T_{50\,\%}$ because a tail voltage will inevitably appear afterward. Although the tail voltage makes the voltage transition smoother in implementation, the worst case is considered in this design phase.

As shown in Fig. 4(c), when damping factor ζ is around 1.5, the initial half of v_{ref} has the most ideally constant slope. Hence, let $\zeta = 1.5$ and then L_{sen} can be derived.

B. Design of the Buffer Stage

The buffer stage should have a high input impedance and a low output impedance. As shown in Fig. 1, a BJT-based class AB amplifier is used as the buffer stage. 300 V, 150 MHz, NPN KSC3503, and PNP KSA1381 are chosen for their high-voltage and high-bandwidth properties. Bias resistors (R_{b1} and R_{b2}) and diodes (D_1 and D_2) are used in the biasing circuit. Emitter resistors (R_{e1} and R_{e2}) are used to avoid thermal runaway.

In prior art, the output stage has a coupled inductor only. A high-value inductance is, thus, required to reduce the loading effect. If the inductance is not sufficiently high, Darlington pairs, which have a high current gain that results in a low output impedance, will be used. However, the bandwidth is compromised with Darlington pairs [23].

In the proposed design, the output stage consists of a resistor R_L and a coupled inductor L_{cm}, which is the primary winding of the CM transformer. The resistive component of the output impedance of a conventional class AB amplifier is much smaller than R_L, and the inductive component is negligible compared to L_{cm}. Consequently, Darlington pairs are not necessary for the proposed buffer stage. Hence, the proposed design has a simpler structure, wider bandwidth, and lower cost.

C. Design of the Output Stage

In the class AB amplifier, the NPN and PNP transistors conduct alternately, and the supply voltage is one-half of the dc link voltage $V_{\rm dc}$. Hence, the power dissipation of the output ACF $P_{\rm loss}$ is expressed as

$$P_{\rm loss} = \frac{1}{T_{sw}} \int_0^{T_{sw}} \frac{1}{2} V_{\rm dc} i_L(t) = \frac{1}{2} V_{\rm dc} |i_L|_{ave} \tag{9}$$

where T_{sw} is the switching period of the inverter. Since the direction of inductor current i_L changes during the operation of the push–pull amplifier, $|i_L|_{ave}$ is the average of the absolute value of i_L.

Given $V_{\rm dc}$ is predefined, a lower $P_{\rm loss}$ can be obtained if i_L is reduced. Since only L_{cm} is used in prior art, i_L can only be reduced by using a high inductance, resulting in a bulky CM transformer.

In the proposed output ACF, a resistor R_L is introduced into the output stage to reset i_L and, thus, reduce $P_{\rm loss}$. The equivalent

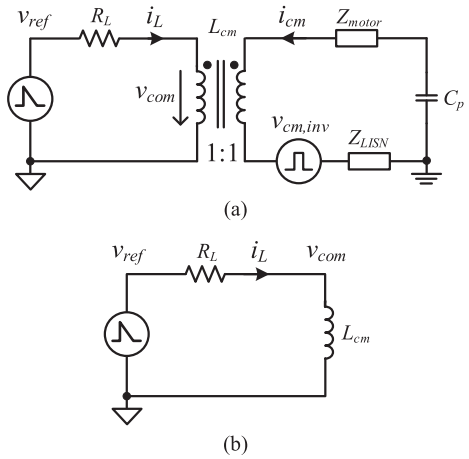

Fig. 5. Equivalent circuit of the output stage. (a) Full model. (b) Simplified model.

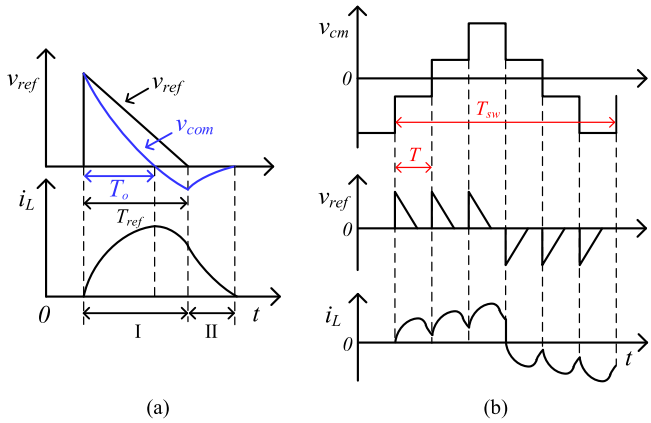

Fig. 6. Waveforms of the output stage. (a) Waveforms excited by a single pulse. (b) Waveforms during a switching cycle.

circuit of the proposed output stage is shown in Fig. 5(a). The voltage across the coupled inductor v_{com} is determined by primary-side and secondary-side excitations, as expressed as

$$v_{com} = L_{cm} \frac{di_L}{dt} + M \frac{di_{cm}}{dt} \tag{10}$$

where M is the mutual inductance.

v_{com} is dominated by the primary side based on two reasons. First, the high inductance of motor windings in the secondary loop mitigates the CM current. Second, the inductance L_{cm} in the proposed design is not very large to avoid bulkiness, which makes the primary-side current dominate the secondary-side current. Thus, Fig. 5(a) can be simplified as Fig. 5(b) to facilitate the circuit design.

Based on Fig. 5(b), i_L is described in (11). The excitation source v_{ref} is a piecewise function. In the first interval ($0 < t < T_{ref}$, where T_{ref} is the reference compensation time), v_{ref} deceases to zero with a constant slope. In the second interval ($t > T_{ref}$), $v_{ref} = 0$. Waveforms of v_{ref}, v_{com}, and i_L are shown in Fig. 6(a)

$$L_{cm} \frac{di_L(t)}{dt} + R_L i_L(t) = v_{ref}(t)$$

$$\begin{cases} v_{ref,\mathrm{I}}(t) = V_m - \frac{V_m}{T_{ref}}t \\ v_{ref,\mathrm{II}}(t) = 0 \end{cases} \tag{11}$$

$$\begin{cases} i_{L,\mathrm{I}}(0) = 0 \\ i_{L,\mathrm{II}}(0) = i_{L,\mathrm{I}}(T_{ref}). \end{cases} \tag{12}$$

When a large R_L is used, i_L will decrease to zero before the next pulse appears, as shown in Fig. 6(a). In such a case, $|i_L|_{ave}$ in (9) can be calculated from a single pulse. On the contrary, if R_L is not sufficiently large to reset i_L, the profiles of i_L in each pulse are not the same. Hence, (12) is revised as (13) to calculate i_L in an iterative way

$$\begin{cases} i_{L,n,\mathrm{I}}(0) = i_{L,n-1,\mathrm{II}}(T - T_{ref}) \\ i_{L,n,\mathrm{II}}(0) = i_{L,n,\mathrm{I}}(T_{ref}) \end{cases} \tag{13}$$

where T is the interval between two pulses and $T = T_{sw}/6$ in this illustration.

It should be noted that different modulation schemes have different switching patterns, and T will also fluctuate in different switching cycles when a specific modulation is in use. For the sake of simplicity, $T = T_{sw}/6$ is taken as an average of different switching patterns in this illustration. When i_L is obtained from (11) and (13), the power consumption of the ACF can be derived according to (9).

Same as $T_{50\%}$ used in the reference stage design to exclude the tail voltage effect, the slope of v_{com} is also calculated from its first half waveform

$$v_{com}(T_{o,50\%}) = L_{cm}\frac{di_L(T_{o,50\%})}{dt} = \frac{1}{2}V_m. \tag{14}$$

Based on (11) and (14), the actual compensation time T_o can be calculated as (15). It is a measure of the slope of CM voltage after compensation

$$T_o = \frac{2L_{cm}}{R_L}\ln\left[\frac{2\left(L_{cm} + R_L T_{ref}\right)}{R_L T_{ref} + 2L_{cm}}\right]. \tag{15}$$

Based on the abovementioned analysis, P_{loss} and T_o are functions of T_{ref}, R_L, and L_{cm} when V_{dc} and T_{sw} are predefined, which can be expressed as

$$\begin{cases} P_{\mathrm{loss}} = f\left(T_{ref}, R_L, L_{cm}\right) \\ T_o = g\left(T_{ref}, R_L, L_{cm}\right). \end{cases} \tag{16}$$

It is challenging to obtain the solution of this multidimensional optimization problem. Hence, the dimensionality reduction method is used to facilitate the design. The first step is to investigate the impact of R_L and L_{cm} on P_{loss} and T_o with a fixed T_{ref}; a local optimum will be found. In the second step, the global optimum is identified by comparing the local optimums calculated from different values of T_{ref}.

Fig. 7 shows the three-dimensional (3-D) curves of P_{loss} and T_o as a function of R_L and L_{cm}, respectively, at a fixed T_{ref}. A larger L_{cm} corresponds to a higher T_o and, thus, smaller *dv/dt*, but the resulting bulky inductor is a concern. A higher R_L can reduce P_{loss}, but T_o will drop; the compensation performance is, thus, compromised. Hence, finding appropriate R_L and L_{cm} is of great importance.

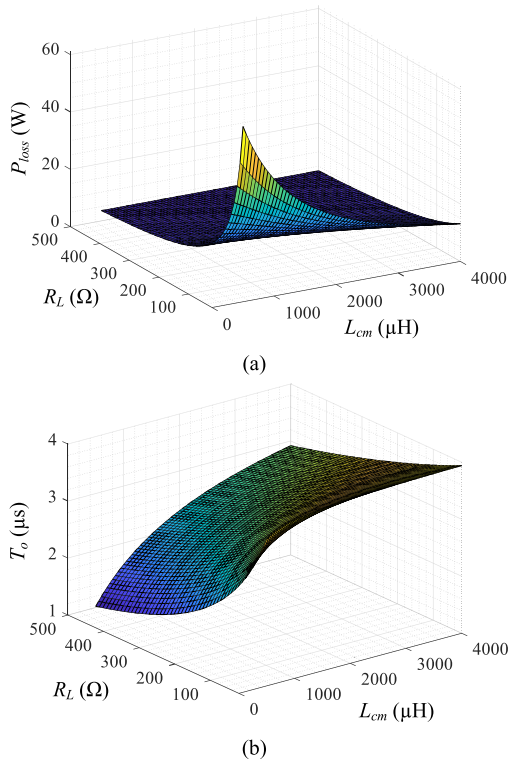

Fig. 7. Three-dimensional curves ($V_{\mathrm{dc}} = 300$ V, $f_{sw} = 10$ kHz, $T_{ref} = 4$ μs). (a) P_{loss} as a function of L_{cm} and R_L. (b) T_o as a function of L_{cm} and R_L.

By drawing different contours, the 3-D curves shown in Fig. 7 are flattened into 2-D curves and combined into one graph, as shown in Fig. 8. The red line and the black line represent P_{loss} and T_o, respectively.

The ACF is used to reduce *dv/dt* and CM current i_{cm} to protect bearings. Bearings of different sizes and materials have different immunity to i_{cm}. The switching frequency f_{sw} also affects the amplitude of i_{cm}. Thus, T_o should be designed according to the requirement of a specific application. For the cases in the early design phase, i_{cm} can be calculated by using EMI prediction methods. For the cases that a prototype is available, one can measure i_{cm} and set a T_o to reduce i_{cm} below a safety level.

Based on (9) and (11), P_{loss} is determined by V_{dc}, f_{sw}, T_{ref}, R_L, and L_{cm}; it does not directly depend on the power rating of motor drive systems. Thus, the abovementioned design procedure for determining filter parameters is applicable for systems of different rated power.

The procedure of selecting the values of R_L and L_{cm} is given as follows.

Step 1: Select P_{loss} and T_o for a specific application.

For example, let P_{loss} accounts for 1% of the total power of the motor drive system. T_o is selected to reduce the peak CM current below a safe level for bearing protection. Since there is currently no standard to regulate the CM current flowing through the motor, the maximum allowable CM current is determined by considering the motor specifications. As a case study, $P_{\mathrm{loss}} =$ 10 W and $T_o = 4$ μs.

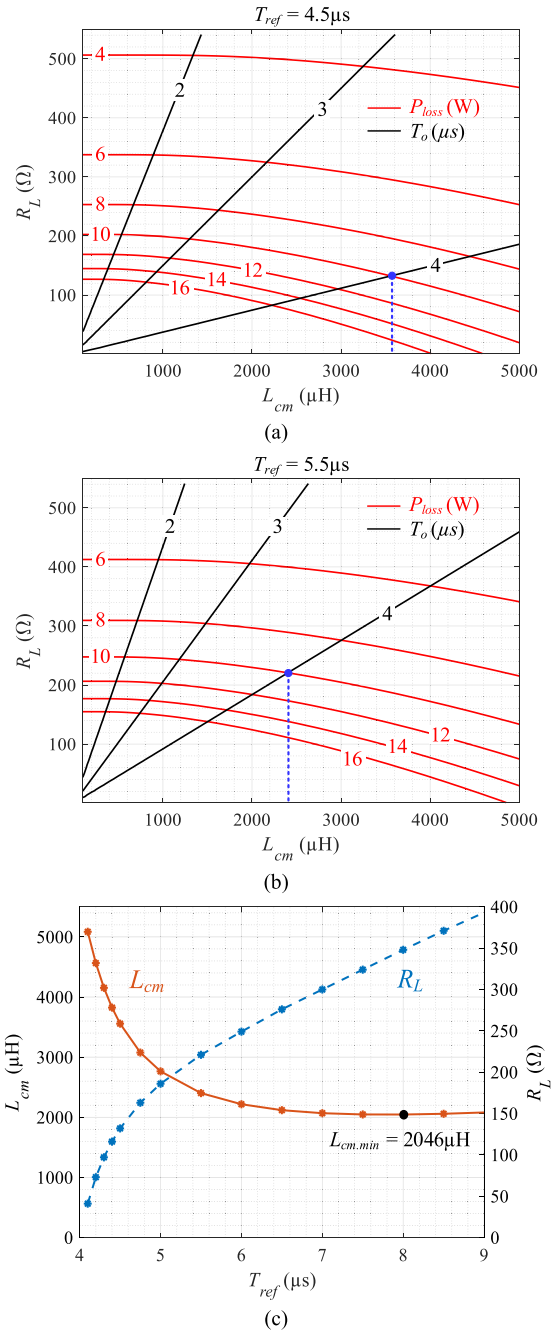

Fig. 8. Parameter design maps ($V_{\rm dc}$ = 300 V, f_{sw} = 10 kHz). (a) T_{ref} = 4.5 μs. (b) T_{ref} = 5.5 μs. (c) T_{ref} varies from 4.1–9 μs.

Step 2: Sweep T_{ref} from a value slightly higher than T_o. Since R_L shares a portion of the compensation voltage, the reference compensation time T_{ref} should be higher than the actual compensation time T_o.

For example, when T_{ref} = 4.5 μs, the blue dot (L_{cm} = 3557 μH, R_L = 132 Ω) fulfills the abovementioned requirements, as shown in Fig. 8(a). When T_{ref} = 5.5 μs, the blue dot moves to another point (L_{cm} = 2402 μH, R_L = 221 Ω), as shown in Fig. 8(b). This illustrates that L_{cm} can be reduced by changing T_{ref} without increasing $P_{\rm loss}$.

TABLE I
COMPONENTS USED IN THE PROPOSED OUTPUT ACF

Components	Value/ Part No.	Components	Value/ Part No.
C_{sen}	100pF × 3	Q_1	KSC3503
R_{sen}	10 kΩ	Q_2	KSA1381
L_{sen}	1.42 mH	R_L	470 Ω
R_{b1}, R_{b2}	41 kΩ	L_{cm} (T37)	2.81 mH
D_1, D_2	1N4148	L_{cm} (HF60)	2.29 mH
C_{DC1}, C_{DC2}	1 μF	T37 core	B64290L0674X037
R_{e1}, R_{e2}	10 Ω	HF60 core	HF60T38X14X22

Step 3: Select optimal values of L_{cm} and R_L based on the results in *Step 2*.

As shown in Fig. 8(c), the required L_{cm} reduces as the increase of T_{ref} and finally falls to a steady level. When T_{ref} = 8 μs, L_{cm} finds its smallest value at 2046 μH. Hence, the optimal values are L_{cm} = 2046 μH and R_L = 348 Ω. In the implementation, values higher than 6 μs are all acceptable since the variation of L_{cm} with T_{ref} becomes insignificant.

As shown in Fig. 8(a) and (b), the red contours closer to the origin of the coordinate axes get denser, implying that the attempt to continuously reduce R_L with a given L_{cm} to pursue better compensation performance will cause high power dissipation. Thus, the proposed output stage consists of R_L and L_{cm}, instead of an inductor L_{cm} only, as in prior art.

III. EXPERIMENTAL VERIFICATION AND DISCUSSION

In order to investigate the effect of different ferrite materials, two CMTs have been fabricated with materials of T37 and HF60. Material T37 has features of low loss factor and high initial permeability ($\mu_{\rm i}$ = 6500) [24]. Material HF60 has low initial permeability ($\mu_{\rm i}$ = 1600) but better high-frequency performance [25]. As shown in Fig. 9(a), the CMTs have one primary winding (L_A) and three secondary windings (L_U, L_V, and L_W). L_A is evenly distributed into three groups so that the coupling factors with three secondary windings are identical.

The photos of the proposed output ACF, the input ACF proposed in [20], and the motor drive system, which is a fan coil unit, have been shown in Fig. 9(b), (c), and (d), respectively. The equipment and connections for EMI measurement are shown in Fig. 9(e). The dc link voltage of the motor drive is 306 V, and the switching frequency is 16 kHz. The values and part numbers of the components used in the output ACF are tabulated in Table I.

A. CM Voltage Compensation by the Output ACF

Fig. 10 shows experimental results of using the CMT fabricated with ferrite material T37. The reference voltage v_{ref} and compensation voltage v_{com} of the proposed output ACF are shown in Fig. 10(a). The CM voltages at the inverter-side $v_{cm,inv,}$ and the motor-side $v_{cm,\rm motor}$ with the output ACF are shown in Fig. 10(b). In order to compare with the passive CM choke, the active circuit of the output ACF is removed;

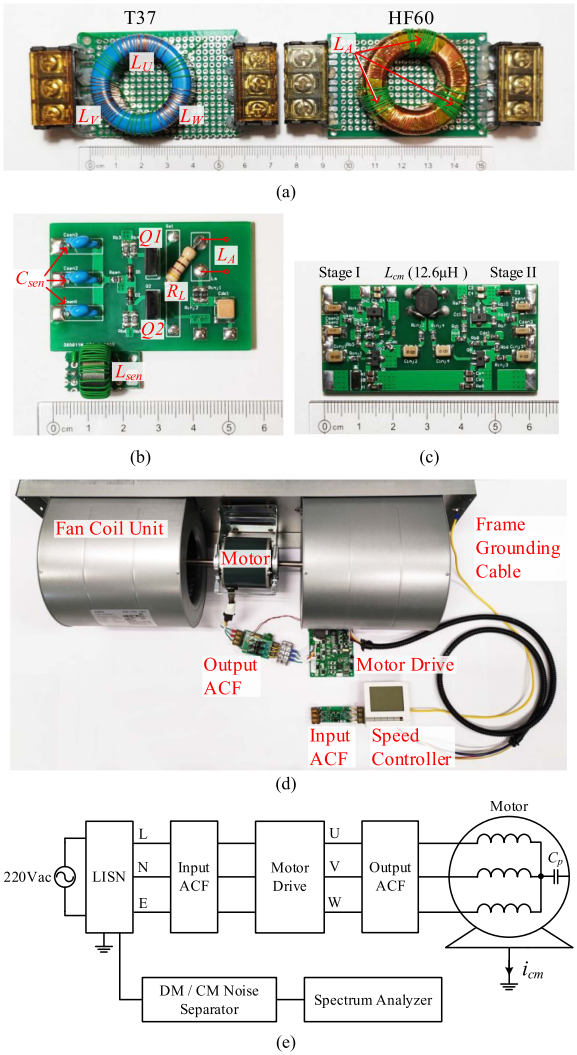

Fig. 9. Setup for CM performance evaluation. (a) CMTs fabricated with ferrite materials of T37 and HF60. (b) Proposed output ACF. (c) Input ACF proposed in [20]. (d) Motor drive system. (e) Equipment and connections for EMI measurement.

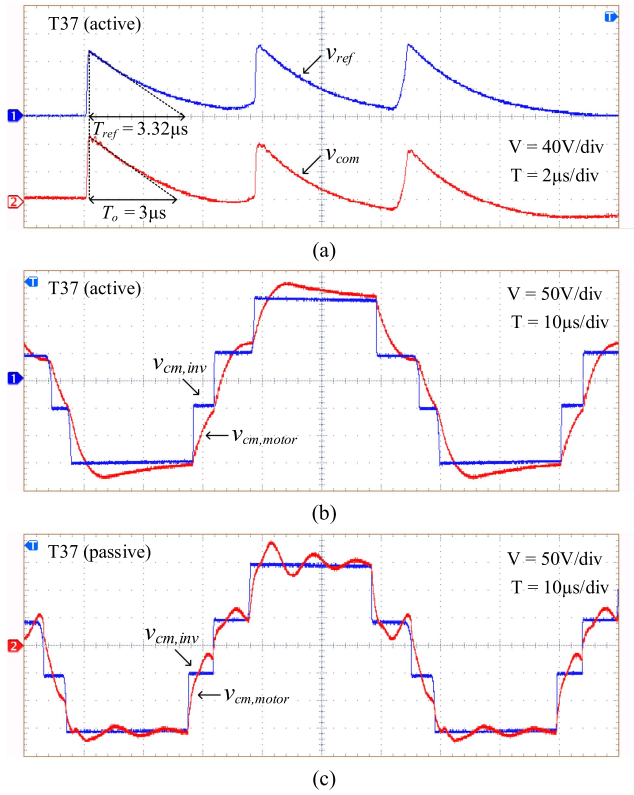

Fig. 10. Waveforms with the CMT fabricated with material T37. (a) v_{ref} and v_{com} of the output ACF. (b) $v_{cm,inv}$ and $v_{cm,\mathrm{motor}}$ with the output ACF. (c) $v_{cm,inv}$ and $v_{cm,\mathrm{motor}}$ with the passive CM choke by removing the active circuit.

waveforms of CM voltage with the passive CM choke are shown in Fig. 10(c).

The CMT of material HF60 has also been tested, and its waveforms are shown in Fig. 11.

As shown in Figs. 10 and 11, the proposed output ACF has increased the rise time of CM voltage from around 100 ns to 3 μs. Passive CM chokes can also slow down *dv/dt*, but their performance is less significant, and resonance in $v_{cm,\mathrm{motor}}$ is observed.

B. CM EMI Spectrum

The CM noise spectra of the motor drive system with the two CMTs (T37 and HF60) under different filtering conditions have been measured, as shown in Fig. 12. The blue lines represent the CM noise spectra without a filter; the red lines show results with a passive CM choke; the yellow lines show results with the proposed output ACF; the purple lines show results with both output and input ACFs. In order to illustrate the insertion loss of the output ACF, the envelopes of the blue and yellow lines are drawn by black lines. The difference between the solid black line and the dashed black line represents the insertion loss of the output ACF. The motor drive system satisfies the EMC standard *IEC 61800-3* [26] with the input and the output ACFs.

It can be seen that the input ACF is most effective in attenuating CM noise. The output ACF has a maximum of 14 dB attenuation higher than the passive CM choke. By using the output ACF, the noise is reduced to within the capacity of the input ACF. Otherwise, the input ACF will saturate when only a CM choke is used at the output side. This issue will be analyzed in Section III-F.

The rise time of CM voltage is increased to 3 μs with the output ACF. A longer rise time can be achieved by increasing T_{ref} and/or decreasing R_L, as analyzed in Section II-C. Then, the output ACF will have better filtering performance, but higher power dissipation will be expected.

C. CM Current Flowing Through the Motor

The waveforms of the CM current flowing through the motor without a filter, with a passive CM choke, and with the output ACF have been shown in Fig. 13. Although the input ACF has good CM filtering performance, it can only attenuate the CM noise injected into the grid, but not the CM current leaked from the motor. Since the damage to bearings is determined by the

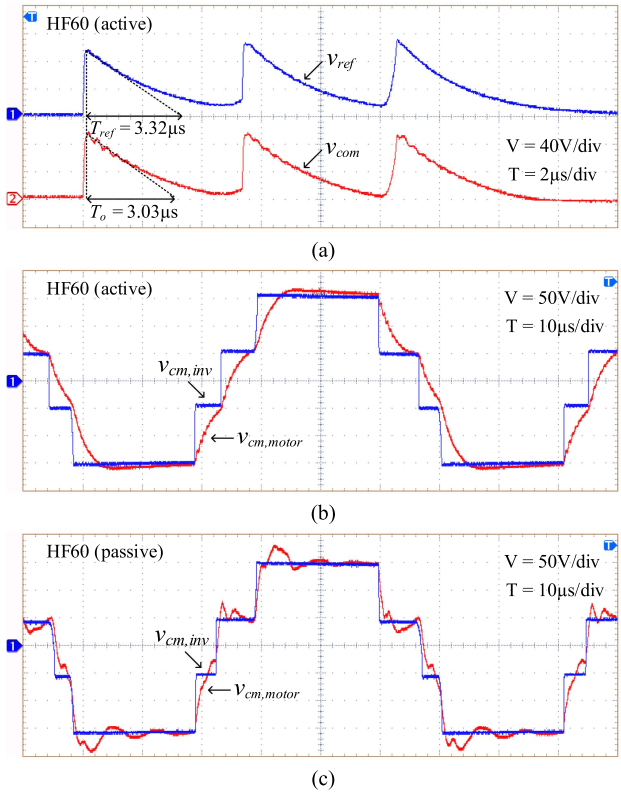

Fig. 11. Waveforms with the CMT fabricated with material HF60. (a) v_{ref} and v_{com} of the output ACF. (b) $v_{cm,inv}$ and $v_{cm,\mathrm{motor}}$ with the output ACF. (c) $v_{cm,inv}$ and $v_{cm,\mathrm{motor}}$ with the passive CM choke by removing the active circuit.

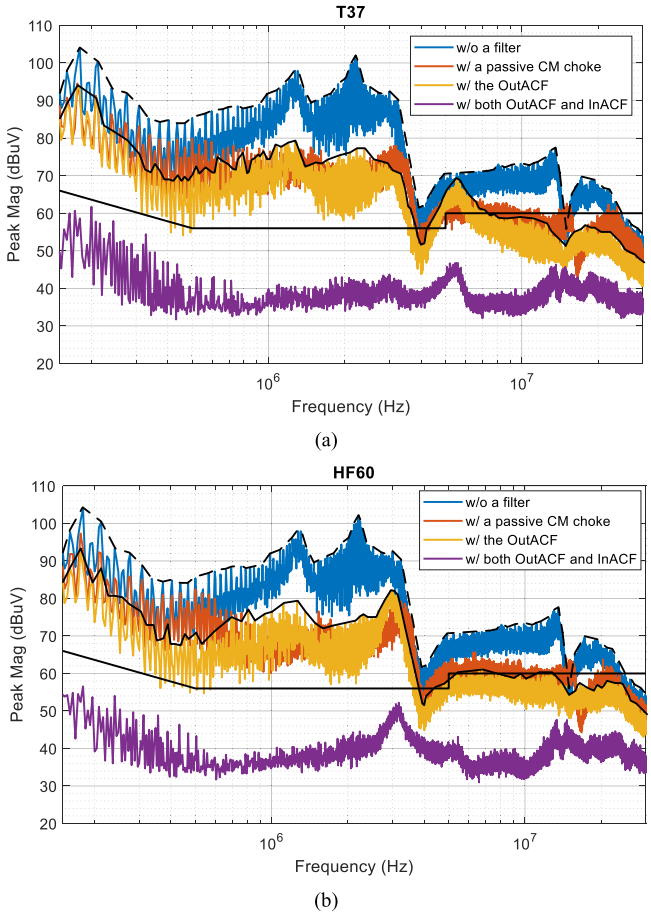

Fig. 12. Peak CM noise spectra of the motor drive system under different filtering conditions. (a) With ferrite material T37. (b) With ferrite material HF60.

peak motor CM current, the peak-to-peak CM current $I_{cm,p\text{-}p}$ have been measured as follows.

The original $I_{cm,p\text{-}p}$ without a filter is 310 mA. $I_{cm,p\text{-}p}$ with a passive CM choke (T37) is 100 mA, which is reduced by 67.7% [(310 mA–100 mA)/310 mA] from its original value. By using the output ACF, $I_{cm,p\text{-}p}$ is further reduced by 30% [(100 mA–70 mA)/100 mA].

The ferrite material HF60 has a slightly better performance than T37. $I_{cm,p\text{-}p}$ with a passive CM choke (HF60) is 90 mA; it is reduced by 70.97% compared to its original value. By using the output ACF, $I_{cm,p\text{-}p}$ is reduced to 65 mA, which is a further reduction of 27.78%. A lower $I_{cm,p\text{-}p}$ can be achieved by increasing T_{ref} and/or decreasing R_L at the cost of increased power dissipation.

D. Investigation Into the Differences Between T37 and HF60

As introduced in the previous sections, the CMT fabricated with ferrite material HF60 has slightly better performance than that with T37. The most important difference is that the output ACF will have a much smaller power dissipation P_{loss} by using HF60 than T37, as shown in Fig. 14.

P_{loss} of the biasing circuit is 0.985 W; it is caused by a high dc link voltage V_{dc} and a small biasing current. According to (9), P_{loss} of the output ACF is determined by $|i_L|_{ave}$. $|i_L|_{ave}$ with the T37 CMT is 33.5 mA, and it is 12.9 mA with the HF60 CMT. There is a 2.6 times higher inductor current with T37 than with

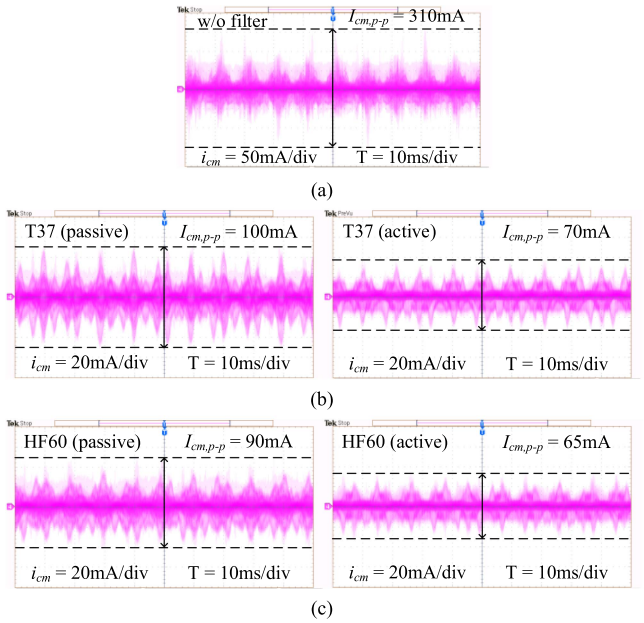

Fig. 13. Waveforms of CM current flowing through the motor. (a) Without a filter. (b) With ferrite material T37. (c) With ferrite material HF60.

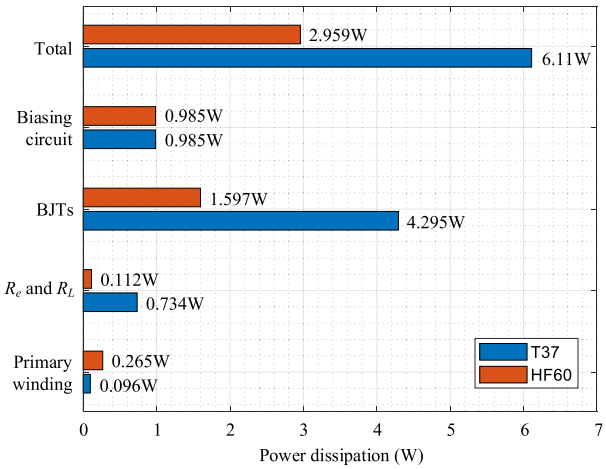

Fig. 14. Power dissipation of the output ACF with ferrite materials T37 and HF60.

HF60. Hence, the output ACF with T37 CMT has higher power dissipation. BJTs consume the largest proportion of $P_{\rm loss}$ since their voltage is equal to $V_{\rm dc}/2$ deducted by a sawtooth edge-compensation waveform, which has a significant rms value.

Contrary to the total power losses with the two types of cores, the $P_{\rm loss}$ of the primary winding with HF60 is 2.76 times higher than that with T37 (265 mW/96 mW = 2.76). The abovementioned experimental results will be investigated as follows.

Since both CMTs (T37 and HF60) are tested with the same circuit, the different inductor currents are caused by the difference in impedance of the CMTs. The equivalent circuits for CM inductors have been analyzed in [27] and [28], as shown in Fig. 15(a). The equivalent circuit of CM inductors is represented by a frequency-dependent inductance $L(f)$, equivalent core loss resistance $R_{\rm core}(f)$, winding loss resistance $R_w(f)$, and winding parasitic capacitance C_w. The small-signal impedance curves of the CMTs are measured by impedance analyzer 4294A, as shown in Fig. 15(b). 4294A can also measure the inductance and ac resistance connected in series, as shown in Fig. 15(c).

Impedance analyzer 4294A displays the inductance and ac resistance of measured impedance by separating the real and imaginary parts. However, the measured ac resistance is not the intrinsic core resistance of the CMT. In order to investigate this issue, an external 100 pF capacitor is paralleled to the T37 CMT. The *L-R* curve with the external capacitor is compared to the original one, as shown in Fig. 16. It is reasonable to observe the self-resonant frequency of impedance shifts to a lower frequency due to increased winding capacitance, but the ac resistance also changes with the additional capacitor. This validates that the ac resistance measured by the impedance analyzer cannot be used to model the $R_{\rm core}(f)$ and $R_w(f)$ in Fig. 15(a).

Since the CMTs fabricated with T37 and HF60 use the same wire gauge and work under the same circuit, the winding loss has a negligible effect on the difference of power dissipation. Instead, the core loss leads to the noticeable difference in power dissipation. In order to investigate the large-signal response of the materials, the magnetic hysteresis loops of T37 and HF60

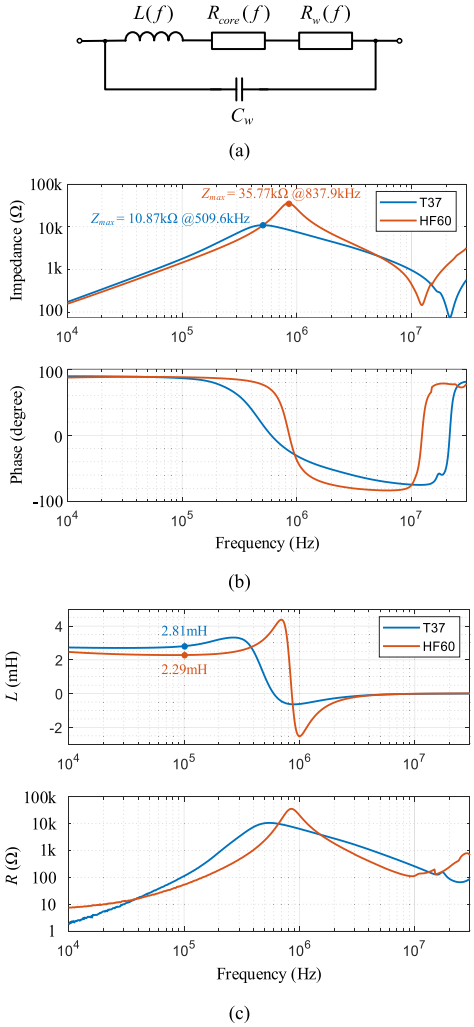

Fig. 15. Impedance characteristics of CM inductors. (a) Equivalent circuit for CM inductors. (b) Impedance curves. (c) Curves of inductance and ac resistance.

have been measured using the methods introduced in [29], as shown in Fig. 17.

According to Fig. 17, the operation of both CMTs has not entered the saturation region upon working with the output ACF. HF60 has a much wider hysteresis loop than T37, implying that HF60 has higher core loss and higher corresponding $R_{\rm core}(f)$. This explains the HF60 CMT has a smaller inductor current. The high-loss feature of HF60, in turn, leads to a lower overall power dissipation of the output ACF. This is different from conventional power inductors in that the low-loss characteristic is preferable.

E. Investigation Into Winding Configuration

Extensive works have been devoted to optimizing the winding design of single-phase inductors and CM chokes. However, the winding configuration of the CMT used in the output ACF that has three conventional secondary windings and a primary winding has not been investigated.

The CMTs tested in the previous sections use symmetrical primary winding configuration. In this section, a new T37 CMT in asymmetrical primary winding configuration has been made,

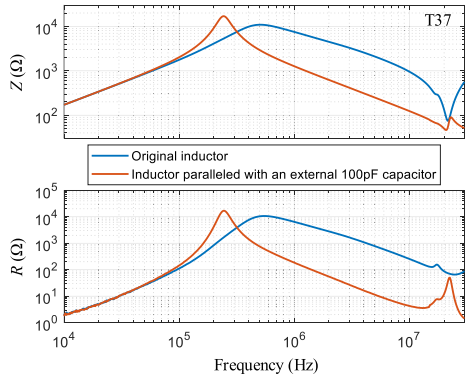

Fig. 16. Impedance characteristics of the CM inductor with and without an external 100 pF capacitor.

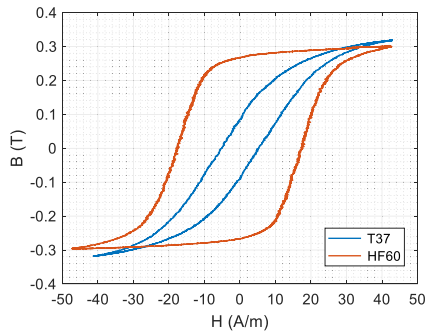

Fig. 17. B-H curves of T37 and HF60 (10 kHz).

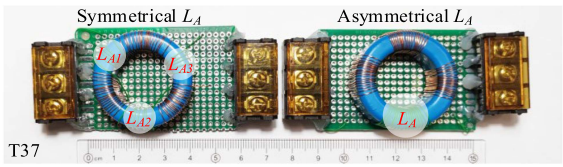

Fig. 18. CMTs of different primary winding configurations.

as shown in Fig. 18, and tested with the same output ACF. Compensation voltage v_{com}, CM current flowing through the motor i_{cm}, and CM noise spectra of the motor drive system with output ACFs in different winding configurations are shown in Fig. 19.

In the asymmetrical CMT, the primary-to-secondary coupling coefficient of one phase is different from the other two. The resulting unbalanced leakage inductance will resonate with motor winding capacitances. Hence, resonance appears in one of the three sawtooth v_{com}, caused by the asymmetrical phase with the variation of the duty cycle. The resulting i_{cm} has a higher peak value (115 mA) than that in symmetrical configuration (70 mA). The CM noise spectra are nearly the same in the low frequency, but a resonant peak around 6 MHz is observed with the asymmetrical CMT.

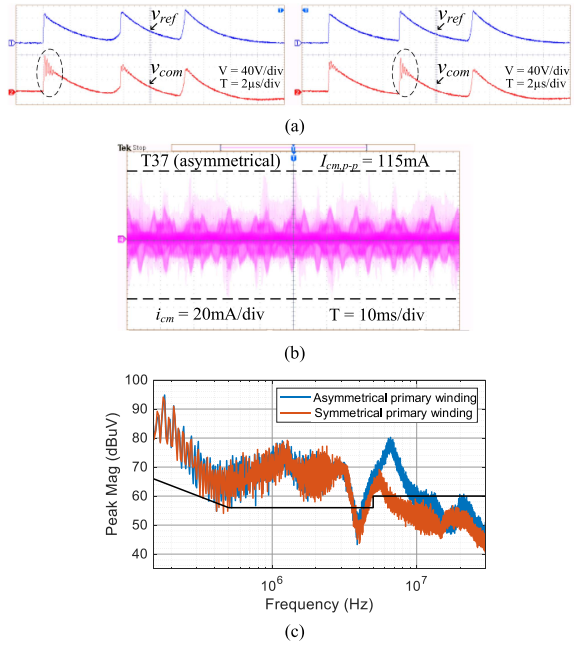

Fig. 19. Waveforms of the CMT with asymmetrical primary winding configuration. (a) v_{ref} and v_{com} of the output ACF in different switching cycles. (b) CM current flowing through the motor. (c) CM noise spectra of the motor drive system with the output ACF in different winding configurations.

TABLE II
COMPARISON OF THE INPUT ACF AND THE OUTPUT ACF

	Input ACF	Output ACF
Objective	★★ Reduce CM noise into the grid	★★ Reduce $I_{cm,peak}$ to protect bearing ★ Reduce CM noise to aid the input ACF
Noise level	Small-signal filter	Large-signal filter
Limiting factor	Saturation due to large v_o swing	Higher power dissipation for a lower dv/dt
Power dissipation	Relatively low - Determined by • Output voltage v_o swing • Peak CM current $I_{cm,peak}$	Relatively high - Determined by • DC link voltage V_{dc} • Compensation time T_o

F. Discussion on the Relationship Between Input and Output ACFs

A comparison of input and output ACFs has been shown in Table II. The input ACF is used to attenuate the CM noise injected into the grid. Since the input ACF cannot attenuate the CM current flowing through the motor, it makes the output ACF is primarily to reduce the motor CM current to protect bearings. The reduction of motor CM current also contributes to a lower CM noise spectrum, which gives aid to the input ACF. Nevertheless, the input ACF is indispensable since it still needs to attenuate the CM noise of the motor drive.

The input ACF is connected at the grid interface where the high-amplitude line-frequency voltage contains small noise. The line-frequency component can be easily excluded by the CM sensing circuit, which makes the input ACF act as a small-signal filter. On the contrary, the output ACF is connected at the output of the inverter, where the CM voltage has high amplitude and steep rising/falling edges. Thus, the output ACF is a large-signal filter.

The output characteristics of the input ACF have been analyzed in [20]; its output voltage v_o is equal to the product

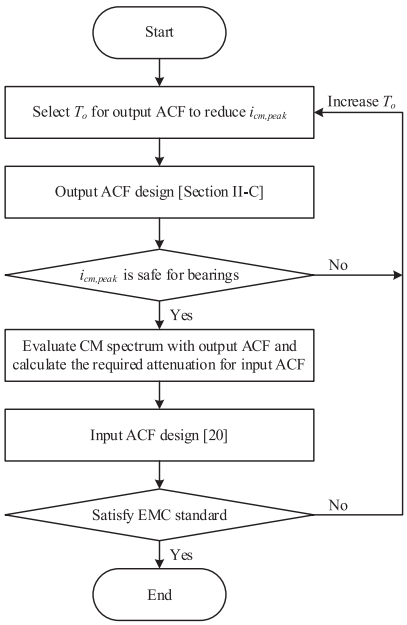

Fig. 20. Flowchart of designing the proposed active CM filtering architecture.

of the sensed CM voltage and a high gain. The amplifier will saturate when v_o swing is higher than the supply voltage. There are several ways to alleviate this issue: a) increase the supply voltage; b) increase the Y-capacitance; c) decrease the voltage gain. This issue can be solved by reducing the CM current with the output ACF. By contrast, the input ACF saturates when only a CM choke is used at the output side.

The limiting factor of the output ACF is power dissipation. Higher power will be consumed to achieve a lower *dv/dt*. Moreover, the increment of power dissipation with the reduction of *dv/dt* is nonlinear; a much higher increment of power consumption is required to further reduce *dv/dt*.

Differences in noise levels leads to differences in power dissipation. The power dissipation of the input ACF is 1.5 W, which is much lower than that of the output ACF. Since class A amplifier is used in the input ACF, the quiescent current should be higher than the peak CM current. The output ACF reduces the CM current, and thus, v_o swing and quiescent current of the input ACF can be reduced, leading to lower power consumption. The power dissipation of the output ACF is mainly determined by dc link voltage $V_{\rm dc}$ and compensation time T_o. Hence, the output ACF will have lower power dissipation in low-voltage motor drive systems; a longer T_o corresponds to a lower *dv/dt* and CM current at the cost of higher power consumption.

The flowchart of designing the proposed active CM filtering architecture is shown in Fig. 20. The first step is to design the output ACF with a selected compensation time T_o to reduce the CM current, as analyzed in Section II-C. T_o will be increased until the peak CM current is reduced to a safe level. The safe level depends on manufacturers and varies from bearing to bearing.

The next step is to evaluate the CM spectrum of the motor drive system with the output ACF, then calculate the required further attenuation for the input ACF to satisfy EMC standards. The design procedures of the input ACF can be found in [20]. If the required attenuation exceeds the capacity of the input ACF, T_o of the output ACF will be increased to aid the input ACF.

The design philosophy is to use the respective advantages of the input and output ACFs to protect bearings and satisfy EMC standards with low power dissipation and small volume.

IV. Conclusion

A new output edge-compensation ACF that compensates for rising/falling edges of CM voltage has been proposed to protect bearings and reduce CM noise. This article is not intended to completely suppress CM noise by the output ACF only regardless of power dissipation; instead, it proposes a holistic CM filtering architecture that utilizes the respective advantages of input and output ACFs to reduce the power dissipation and physical volume. Characteristics and design considerations of the ACFs for motor drives are summarized as follows.

1) The input ACF is a small-signal filter, while the output ACF is a large-signal one. The input ACF can achieve high attenuation with lower power consumption and smaller volume. The output ACF can reduce *dv/dt* at motor terminals and protect bearings while the input ACF cannot.
2) The power dissipation of the output ACF mainly depends on $V_{\rm dc}$ and T_o. $V_{\rm dc}$ determines the magnitude of CM voltage, and T_o regulates the compensation effect. The increment of power dissipation is much higher than that of T_o. High power loss will result in requiring bulky heatsinks and, thus decreasing overall power density. Hence, *dv/dt* is reduced but not eliminated with the proposed output ACF.
3) Ferrite materials significantly affect the power consumption of the output ACF. The high-loss ferrite material HF60 has a higher large-signal ac resistance, which reduces the current and power dissipation of the output ACF.
4) The primary winding of the CMT used in the output ACF should have a symmetrical configuration to achieve identical coupling with secondary windings.

References

[1] M. H. Rashid, *Power Electronics Handbook*. Oxford, U.K.: Butterworth-Heinemann, 2017.
[2] A. Muetze and A. Binder, "Calculation of circulating bearing currents in machines of inverter-based drive systems," *IEEE Trans. Ind. Electron.*, vol. 54, no. 2, pp. 932–938, Apr. 2007.
[3] M. Mechlinski, S. Schroder, J. Shen, and R. W. De Doncker, "Grounding concept and common-mode filter design methodology for transformerless MV drives to prevent bearing current issues," *IEEE Trans. Ind. Appl.*, vol. 53, no. 6, pp. 5393–5404, Nov./Dec. 2017.
[4] T. Plazenet, T. Boileau, C. Caironi, and B. Nahid-Mobarakeh, "A comprehensive study on shaft voltages and bearing currents in rotating machines," *IEEE Trans. Ind. Appl.*, vol. 54, no. 4, pp. 3749–3759, Jul./Aug. 2018.
[5] R. D. S. Araujo, R. D. A. Rodrigues, H. de Paula, B. J. C. Filho, L. M. R. Baccarini, and A. V. Rocha, "Premature wear and recurring bearing failures in an inverter-driven induction motor—Part II: The proposed solution," *IEEE Trans. Ind. Appl.*, vol. 51, no. 1, pp. 92–100, Jan./Feb. 2015.
[6] D. Jiang, Z. Shen, and F. Wang, "Common-Mode voltage reduction for paralleled inverters," *IEEE Trans. Power Electron.*, vol. 33, no. 5, pp. 3961–3974, May 2018.
[7] J. Xue, F. Wang, X. Zhang, D. Boroyevich, and P. Mattavelli, "Design of output passive EMI filter in DC-fed motor drive," in *Proc. IEEE Appl. Power Electron. Conf. Expo.*, 2012, pp. 634–640.
[8] V. Dzhankhotov and J. Pyrhonen, "Passive LC filter design considerations for motor applications," *IEEE Trans. Ind. Electron.*, vol. 60, no. 10, pp. 4253–4259, Oct. 2013.

[9] M. H. Hedayati, A. B. Acharya, and V. John, "Common-Mode filter design for PWM rectifier-based motor drives," *IEEE Trans. Power Electron.*, vol. 28, no. 11, pp. 5364–5371, Nov. 2013.
[10] D. Menzi, D. Bortis, and J. W. Kolar, "EMI filter design for a three-phase buck-boost Y-Inverter VSD with unshielded motor cables considering IEC 61800-3 conducted & radiated emission limits," *IEEE Trans. Power Electron.*, vol. 36, no. 11, pp. 12919–12937, Nov. 2021.
[11] S. Wang, Y. Y. Maillet, F. Wang, D. Boroyevich, and R. Burgos, "Investigation of hybrid EMI filters for common-mode EMI suppression in a motor drive system," *IEEE Trans. Power Electron.*, vol. 25, no. 4, pp. 1034–1045, Apr. 2010.
[12] S. Takahashi, S. Ogasawara, M. Takemoto, K. Orikawa, and M. Tamate, "Common-Mode voltage attenuation of an active common-mode filter in a motor drive system fed by a PWM inverter," *IEEE Trans. Ind. Appl.*, vol. 55, no. 3, pp. 2721–2730, May/Jun. 2019.
[13] Y. Zhang, Q. Li, and D. Jiang, "A motor CM impedance based transformerless active EMI filter for DC-Side common-mode EMI suppression in motor drive system," *IEEE Trans. Power Electron.*, vol. 35, no. 10, pp. 10238–10248, Oct. 2020.
[14] S. Ogasawara, H. Ayano, and H. Akagi, "An active circuit for cancellation of common-mode voltage generated by a PWM inverter," *IEEE Trans. Power Electron.*, vol. 13, no. 5, pp. 835–841, Sep. 1998.
[15] M. C. D. Piazza, G. Tine, and G. Vitale, "An improved active common-mode voltage compensation device for induction motor drives," *IEEE Trans. Ind. Electron.*, vol. 55, no. 4, pp. 1823–1834, Apr. 2008.
[16] M. C. D. Piazza, A. Ragusa, and G. Vitale, "An optimized feedback common mode active filter for vehicular induction motor drives," *IEEE Trans. Power Electron.*, vol. 26, no. 11, pp. 3153–3162, Nov. 2011.
[17] W. Chen, X. Yang, J. Xue, and F. Wang, "A novel filter topology with active motor CM impedance regulator in PWM ASD system," *IEEE Trans. Ind. Electron.*, vol. 61, no. 12, pp. 6938–6946, Dec. 2014.
[18] M. C. D. Piazza, M. Luna, and G. Vitale, "EMI reduction in DC-Fed electric drives by active common-mode compensator," *IEEE Trans. Electromagn. Compat.*, vol. 56, no. 5, pp. 1067–1076, Oct. 2014.
[19] S. Ohara, S. Ogasawara, T. Masatsugu, K. Orikawa, and Y. Yamamoto, "A novel active common-noise canceler combining feedforward and feedback control," in *Proc. IEEE Energy Convers. Congr. Expo.*, 2017, pp. 2469–2475.
[20] K. Zhang, K. W. Wang, and H. S. H. Chung, "High-Attenuation wideband active common-mode EMI filter section," *IEEE Trans. Power Electron.*, vol. 37, no. 5, pp. 5479–5490, May 2022.
[21] D. Busse, J. Erdman, R. J. Kerkman, D. Schlegel, and G. Skibinski, "Bearing currents and their relationship to PWM drives," *IEEE Trans. Power Electron.*, vol. 12, no. 2, pp. 243–252, Mar. 1997.
[22] A. Muetze, A. Binder, H. Vogel, and J. Hering, "What can bearings bear?," *IEEE Ind. Appl. Mag.*, vol. 12, no. 6, pp. 57–64, Nov./Dec. 2006.
[23] J. Millman and A. Grabel, *Microelectronics*. New York, NY, USA: McGraw-Hill, 1987.
[24] TDK Electronics, "Ferrites and accessories," SIFERRIT material T37 Datasheet, May. 2017. [Online]. Available: https://www.tdk-electronics.tdk.com/download/528874/1b641f57f03d5cb0cc6cd79f9792bc9c/pdf-t37.pdf
[25] TDK Electronics, "Ferrite cores for EMI suppression," Material characteristics datasheet, Jan. 2021. [Online]. Available: https://product.tdk.com/system/files/dam/doc/product/ferrite/ferrite/ferrite-core/catalog/ferrite_emc_material_characteristics_en.pdf
[26] *Adjustable Speed Electrical Power Drive Systems - Part 3: EMC Requirements and Specific Test Methods*, IEC61800-3, International Electrotechnical Commission, Geneva, Switzerland, Sep. 2018.
[27] M. L. Heldwein, L. Dalessandro, and J. W. Kolar, "The three-phase common-mode inductor: Modeling and design issues," *IEEE Trans. Ind. Electron.*, vol. 58, no. 8, pp. 3264–3274, Aug. 2011.
[28] S. Takahashi and S. Maekawa, "Wideband small-signal model of common-mode inductors based on stray capacitance estimation method," *IEEJ J. Ind. Appl.*, vol. 11, pp. 514–521, 2021.
[29] TDK Electronics, "MnZn Ferrite Material," EPCOS N87 datasheet, Sep. 2018. [Online]. Available: https://www.netl.doe.gov/sites/default/files/netl-file/Core-Loss-Datasheet---MnZn-Ferrite---N87%5B1%5D.pdf

Kun Zhang (Member, IEEE) received the B.Eng. degree from Wuhan University, Wuhan, China, and the Ph.D. degree from the City University of Hong Kong, Kowloon, Hong Kong, in 2018 and 2022, respectively, all in electrical engineering.

His current research interests include active EMI filtering techniques, power factor correction, and stability analysis of power converters.

Henry Shu-Hung Chung (Fellow, IEEE) received the B.Eng. and Ph.D. degrees in electrical engineering from Hong Kong Polytechnic University, Hong Kong, in 1991 and 1994, respectively.

Since 1995, he has been with the City University of Hong Kong, where he is currently the Dean of Students, a Chair Professor with the Department of Electrical Engineering, and the Director of the Centre for Smart Energy Conversion and Utilization Research. He has edited one book, authored eight research book chapters, and more than 460 technical papers including 220 refereed journal papers in his research areas, and holds 80 patents. His current research interests include renewable energy conversion technologies, lighting technologies, energy harvesting, smart grid technologies, and computational intelligence for power electronic systems.

Dr. Chung was recipient of 2021 IEEE Power Electronics Society R. David Middlebrook Achievement Award. He was the recipient of CityU Outstanding Research Award in 2020 and CityU Teaching Excellence Awards in 2018 and 2022, respectively. He is currently an Associate Editor for the IEEE TRANSACTIONS ON POWER ELECTRONICS and the IEEE JOURNAL OF EMERGING AND SELECTED TOPICS IN POWER ELECTRONICS. He was the Editor-in-Chief of the IEEE Power Electronics Letters 2014–2018. He was also the Chair of the Technical Committee of the High-Performance and Emerging Technologies, IEEE Power Electronics Society in 2010–2014. He was the recipient of numerous industrial awards for his invented energy saving technologies.

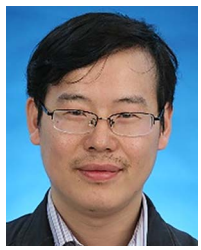

Weimin Wu (Member, IEEE) received the Ph.D. degrees in electrical engineering from the College of Electrical Engineering, Zhejiang University, Hangzhou, China, in 2005.

He was a Research Engineer with the Delta Power Electronic Center, Shanghai, from Jul. 2005–Jun. 2006. Since Jul. 2006, he has been a Faculty Member with Shanghai Maritime University, where he is currently a Full Professor in Department of Electrical Engineering. He was a Visiting Professor with the Center for Power Electronics Systems, Virginia Polytechnic Institute, and State University, Blacksburg, USA, from Sep. 2008 to Mar. 2009. From Nov. 2011 to Jan. 2014, he was also a visiting professor with the Department of Energy Technology, Aalborg University, Demark, working at the Center of Reliable Power Electronics. He has coauthored more than 200 papers and holds 15 patents. His research interests include power converters for renewable energy systems, power quality, smart grid, and energy storage technology.

Dr. Wu is an Associate Editor for IEEE TRANSACTIONS ON INDUSTRY ELECTRONICS.